

Measurement of Local Deformation due to Lung Tumor Response to Radiation Therapy

Geoffrey D. Hugo¹, Kunlin Cao², Christopher Guy¹, Elisabeth Weiss¹, Nuzhat Jan¹, and Gary E. Christensen³

¹ Department of Radiation Oncology, Virginia Commonwealth University, Richmond, VA 23298, USA,

gdhugo@vcu.edu

² Biomedical Image Analysis Lab, GE Global Research Center, Niskayuna, NY 12309, USA,

³ Department of Electrical and Computer Engineering, University of Iowa, Iowa City, IA 52242, USA

Abstract. Accurate alignment of intra-subject CT acquired during radiotherapy is challenging due to tumor regression introducing large image content differences. Some regressing tumors tend to expose newly-visible lung parenchyma, in a type of regression we term ‘infiltrative’. We evaluated two nonrigid registration algorithms for accuracy and plausibility in aligning two images demonstrating infiltrative regression. Both used a vesselness measure-based feature cost and a linear elastic penalty term. The performance of sum of square difference and sum of square tissue volume difference intensity costs were compared in three subjects. Landmark error was not significantly different between the two algorithms, although sum of square tissue volume difference produced more plausible transformations in the infiltrative regression scenario.

Keywords: image registration, computed tomography, response, microscopic extension, lung cancer

1 Introduction

Lung tumors routinely exhibit regression in response to radiotherapy, with evident reduction in volume visible on computed tomography (CT) imaging within the first few weeks of therapy [1–4]. At the end of a treatment course – generally six or seven weeks – the tumor volume measured on CT, on average for the population, is roughly half of that measured during simulation. However, tumor volume response varies widely across patients, with some small number of tumors progressing in size and others with a large response of over 80% regression by volume [1]. It is not currently possible to predict the amount of tumor regression for a particular patient prior to therapy.

Tumor volume regression can introduce large changes in the relative position of adjacent tissue. While much of this tissue is normal, it contains pockets of

microscopic extension of the lung tumor, which is not visible on macroscopic imaging such as CT or PET. The standard of practice in radiotherapy is to expand the visible tumor by a fixed margin (often 5 to 8 mm) during initial planning to account for this subclinical disease with a prescribed radiation dose. Accurate monitoring of the location of this ‘rind’ of tissue throughout the treatment course is important for estimation of the delivered radiation dose and for localization of the targets for dose delivery. However, since the subclinical disease is not visible, changes in the location during therapy must be inferred through registration.

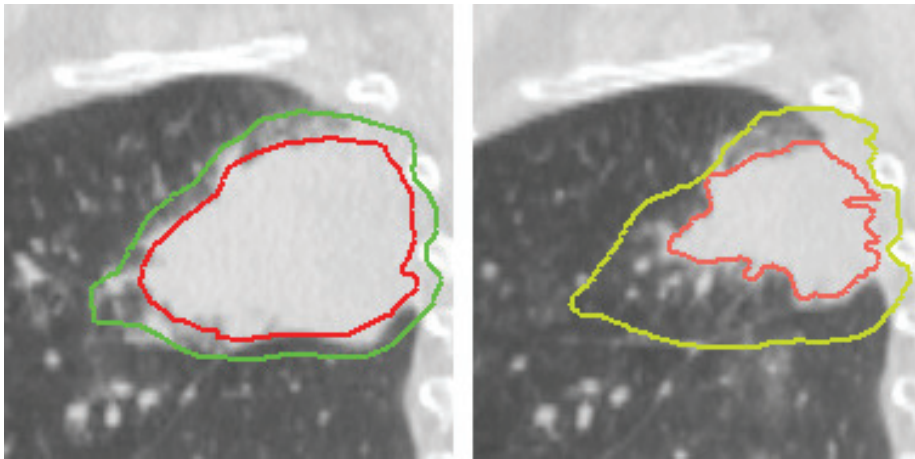


Fig. 1. An example of tumor regression relative to adjacent vasculature. Left, planning image with the gross tumor shown in red and the subclinical target shown in green. Right, mid-treatment image with the residual gross tumor shown in red and the subclinical target shown in yellow. The subclinical target boundary was located using the method of [5]. The distance between the tumor boundary and surrounding vasculature has increased due to ‘infiltrative type’ tumor regression.

Recently, it has been shown that the border regions of lung tumors often regress relative to adjacent normal tissue such as pulmonary vessels [5, 6]. We follow the method of [7] and distinguish between two types of tumor regression. In ‘infiltrative’ type regression, the tumor border appears to regress in relation to the adjacent normal tissue (see Fig. 1). A hypothesis to explain this type of regression is that the lung tumor grows diffusely into the adjacent tissue, without displacing large structures such as vessels. As the tumor begins to disintegrate in response to radiation, relatively large normal tissue structures such as vessels are left intact. In this manner, new lung parenchyma is exposed where tumor tissue was previously. In ‘encapsulated’ type regression, adjacent tissue will regress elastically with the tumor boundary. In this hypothesis, tumor growth elastically displaces adjacent lung tissue, which then elastically decompresses as the tumor

regresses. Tumors of both regression subtypes have been observed [5, 6]. For infiltrative type regression, the tumor border is not a good surrogate for the position of the adjacent tissue and, therefore, of the microscopic extension, so a registration algorithm which focuses on aligning the high-contrast boundary of the tumor and interpolating in adjacent regions will misalign these sections.

In [5], manual landmarks and deformable registration in the region directly surrounding the subclinical target boundary were used to estimate the location of the boundary, but the accuracy of the registration inside the entire normal lung tissue region was not assessed. In [8], the difference of transforms from intensity-driven registration with and without the tumor masked was used to estimate the regression type, but the registration was unregularized and registration accuracy was not quantified. In [9], a rigidity penalty was used within the tumor to prevent non-physiological deformations, but the goal of that work was to align normal lung tissue, so the plausibility of the registration around and within the tumor was not evaluated.

The goal of this study is to design a registration strategy to provide accurate correspondence in the lung tissue adjacent to the tumor, independent of the regression type. To do so, we compare two algorithms that both use an intensity cost and a cost based on enhancing vessel-like features. For one of the algorithms, we use an intensity cost that accounts for varying image intensity due to tissue volume changes, to determine if such a cost function can better model deformation in the context of tumor regression than a more conventional sum of square intensity difference cost. We evaluate each algorithm using physician-defined point landmarks and by visualizing plausibility of the transform.

2 Method

2.1 Patient data acquisition and preprocessing

From a previous IRB-approved study of repeat computed tomography (CT) images (Philips Brilliance Big Bore, Fitchburg, WI) in radiotherapy patients, three subjects with visually-identified infiltrative type regression were selected. Each patient was imaged at the time of radiotherapy simulation and once during radiotherapy. Active breathing control [2] was used to produce a consistent breath hold at end of normal inspiration during imaging. CT voxel size was [1.2, 1.2, 2.0] mm in two patients and [1.2, 1.2, 3.0] mm in one patient. A radiation oncologist manually delineated both lungs; the tumor was included in the labeled lung region. Tumor-bearing regions were contoured separately by the same physician.

2.2 Image registration

The ability to accurately align intra-subject CT images of the lung with infiltrative-type tumor regression was evaluated using two different registration algorithms. Algorithm A and B differ from each other by the way they define intensity correspondence. Algorithm A registers two images by matching the intensities of

the two images while Algorithm B registers two images by matching the tissue volumes which is calculated from the image intensities. In addition to matching image intensities, both algorithms match corresponding vessel features and use the same regularization cost.

Algorithm A: sum of squared intensity difference within the lung and tumor Algorithm A uses a sum of squared difference (SSD) intensity-based similarity cost to match the intensities within a mask region containing the lung and tumor tissue defined on each image separately. The SSD cost is defined as

$$C_{SSD} = \sum_{\mathbf{x} \in \Omega} [I_m(\mathbf{h}(\mathbf{x})) - I_f(\mathbf{x})]^2, \quad (1)$$

where I_f and I_m are the fixed and moving images, respectively, $\mathbf{h}(\mathbf{x})$ is the transformation that maps the moving to the fixed image, and $\Omega \subset \mathbb{R}^3$ is the union of the regions containing both lung and tumor in the fixed and deformed moving images. In this study, the planning image was chosen as I_f and the mid-treatment image as I_m .

Pulmonary vasculature serves as an easily distinguishable and highly specific feature for image registration. However, due to the relatively low contrast of small vessels compared to high-contrast boundaries such as the lung / chest wall and lung / tumor interfaces, intensity-based cost functions are generally insensitive to match these features. Using a similar strategy as in [10], we used a filter-based method to highlight tube-shaped objects in the lung regions. The vesselness measure gives the probability $[0, 1]$ that a voxel is contained within a tube-shaped object. To generate the vesselness measure from each image, we employed the approach in [11]. To calculate the vesselness measure, we calculate a matrix of second-order directional derivatives, termed the Hessian matrix, at each voxel location to evaluate the local curvature of the image in three-dimensional space. A tube, or vessel, is ideally represented as having low curvature along the longitudinal axis of the vessel and high curvature along the two orthogonal axes. Eigen decomposition of this matrix enables evaluation of the second order structure around the voxel of interest for arbitrary orientations, which eliminates the need for derivative filters oriented along the direction of the vessel. Instead, the eigenvalues represent the curvature along the principal axes of the vessel. After ordering the eigenvalues by magnitude $|\lambda_1| \leq |\lambda_2| \leq |\lambda_3|$, a vessel is optimally represented as having the two largest eigenvalues nearly equal, with both having very large magnitude in relation to the third eigenvalue. Thus, the vesselness measure is calculated as

$$F(\lambda) = \begin{cases} (1 - e^{-\frac{R_A^2}{2\alpha^2}}) \cdot e^{-\frac{R_B^2}{2\beta^2}} \cdot (1 - e^{-\frac{S^2}{2\rho^2}}) & \text{if } \lambda_2 < 0 \text{ and } \lambda_3 < 0 \\ 0 & \text{otherwise} \end{cases} \quad (2)$$

with $R_A = \frac{|\lambda_2|}{|\lambda_3|}$, $R_B = \frac{|\lambda_1|}{\sqrt{|\lambda_2\lambda_3|}}$, $S = \sqrt{\lambda_1^2 + \lambda_2^2 + \lambda_3^2}$ where R_A distinguishes between plate-like and tubular structures, R_B accounts for the deviation from a

blob-like structure, and S differentiates between tubular structure and noise. α , β , ρ control the sensitivity of the vesselness measure. The experiments in this paper use $\alpha = 0.5$, $\beta = 0.5$, and $\rho = 5$.

The vesselness measure for each image, $F_f(\mathbf{x})$ and $F_m(\mathbf{x})$ for the fixed and moving images, respectively, was calculated, and the sum of square vesselness measure difference (SSVMD) cost is

$$C_{SSVMD} = \sum_{\mathbf{x} \in \Omega} [F_m(\mathbf{h}(\mathbf{x})) - F_f(\mathbf{x})]^2, \quad (3)$$

where Ω is the region containing only lung parenchyma.

To smooth the transformation and penalize non-physiological deformations, a Laplacian regularizer was employed. The regularization term in the cost function is

$$C_{REG} = \int_{\Omega} \|\nabla^2 \mathbf{u}(\mathbf{x})\|^2 d\mathbf{x} \quad (4)$$

where $\mathbf{u}(\mathbf{x}) = \mathbf{h}(\mathbf{x}) - \mathbf{x}$ is the displacement field, and $\nabla^2 = \nabla \cdot \nabla = \left[\frac{\partial^2}{\partial x_1^2} + \frac{\partial^2}{\partial x_2^2} + \frac{\partial^2}{\partial x_3^2} \right]$.

The total cost used in this algorithm is then given by

$$C_A = C_{SSD} + \rho_v C_{SSVMD} + \rho_r C_{REG} \quad (5)$$

where ρ_v and ρ_r are weighting factors that control the contribution of each cost term.

A cubic B-spline basis was selected to parameterize the transform $\mathbf{h}(\mathbf{x})$ due to its ability to represent non-rigid tissue changes in a compact form, which enables computational efficiency. With B-splines, the transform is represented by

$$\mathbf{h}(\mathbf{x}) = \mathbf{x} + \sum_{\mathbf{k} \in K} \phi_{\mathbf{k}} \beta(\mathbf{x} - \mathbf{x}_i), \quad (6)$$

where $\phi_{\mathbf{k}}$ is the coefficient vector of the k -th control point \mathbf{x}_i , K is the spline lattice, and $\beta(x)$ is the cubic B-spline basis function.

Algorithm B: sum of squared tissue volume difference within the lung and tumor

Algorithm B is the same as Algorithm A except that the SSD similarity cost is replaced by an intensity cost which accounts for changes in voxel intensity due to local tissue volume changes. The sum of squared tissue volume difference (SSTVD) cost is based on the hypothesis that lung parenchyma image intensity can be approximated as a linear combination of air and tissue [12, 13]. The tissue volume contained in a voxel can be estimated by scaling the voxel volume by a linear function of image intensity in Hounsfield Units (HU). The SSTVD cost is the sum of square differences of the tissue volume at each location given by

$$C_{SSTVD} = \int_{\Omega} [V_f(\mathbf{x}) - V_m(\mathbf{h}(\mathbf{x}))]^2 d\mathbf{x}$$

$$= \int_{\Omega} \left[v_f(\mathbf{x}) \frac{I_f(\mathbf{x}) + 1000}{1055} - v_m(\mathbf{h}(\mathbf{x})) \frac{I_m(\mathbf{h}(\mathbf{x})) + 1000}{1055} \right]^2 d\mathbf{x} \quad (7)$$

where $\frac{I(\mathbf{x})+1000}{1055} = \frac{I(\mathbf{x})-HU_{air}}{HU_{tissue}-HU_{air}}$, and Ω was the union of the region containing the lungs and tumor (the same region used for SSD cost in Alg. A). The volume of a voxel in the moving image varies with the transformation $\mathbf{h}(\mathbf{x})$. The Jacobian of the transformation estimates local volume change, so the moving image voxel volume is evaluated as $v_m(\mathbf{h}(\mathbf{x})) = v_f(\mathbf{x}) \cdot J(\mathbf{h}(\mathbf{x}))$. The total cost used in this algorithm is then given by

$$C_A = C_{SSTVD} + \rho_v C_{SSVMD} + \rho_r C_{REG}. \quad (8)$$

2.3 Experiments and analysis

Registration performance was evaluated by comparison to physician-defined homologous point landmarks. Landmarking was performed using the software package IX [14]. 100 point landmarks were automatically identified inside the lung on the fixed image using a feature descriptor based on image intensity and intensity gradient magnitude, culled from a larger set of points to ensure an even and well-spaced distribution throughout the lungs. A radiation oncologist then manually located the landmark in the moving image. IX includes a feature to assist manual landmarking based on a thin plate spline fit of a training set of manually-located landmark pairs, but this feature was not used; all landmarks in the moving image were manually located.

After registration, the resulting transformation from each registration algorithm A and B was used to transform the coordinates of the fixed landmarks into the moving image domain. Landmark registration error was evaluated as the distance between the transformed fixed landmark and the moving landmark.

In addition to quantifying registration accuracy at landmarks, we evaluated the plausibility of each transformation by reviewing the local tissue deformations. The Jacobian determinant of the transformation (termed the ‘‘Jacobian’’ here) at a point represents local expansion or contraction of the tissue. The Jacobian of transform $\mathbf{h}(\mathbf{x})$ is defined as

$$J(\mathbf{h}(\mathbf{x})) = \begin{vmatrix} \frac{\partial h_1(\mathbf{x})}{\partial x_1} & \frac{\partial h_1(\mathbf{x})}{\partial x_2} & \frac{\partial h_1(\mathbf{x})}{\partial x_3} \\ \frac{\partial h_2(\mathbf{x})}{\partial x_1} & \frac{\partial h_2(\mathbf{x})}{\partial x_2} & \frac{\partial h_2(\mathbf{x})}{\partial x_3} \\ \frac{\partial h_3(\mathbf{x})}{\partial x_1} & \frac{\partial h_3(\mathbf{x})}{\partial x_2} & \frac{\partial h_3(\mathbf{x})}{\partial x_3} \end{vmatrix}. \quad (9)$$

A $J(\mathbf{h}(\mathbf{x}))$ value less than one corresponds to a situation where points mapped from the domain of the fixed image near \mathbf{x} contract locally under the transformation. $J(\mathbf{h}(\mathbf{x}))$ greater than one corresponds with expansion, and an identity value implies no expansion or contraction.

3 Results

Fig. 2 shows the moving image overlaid on the fixed image before and after registration with each algorithm. Alg. A (SSD) visually produces a good regis-

tration of the lung boundaries and vasculature. The algorithm also aligns the tumor boundary. However, in the case of infiltrative regression, the boundary is receding away from the original position, exposing newly-visible parenchymal tissue which is present in the moving but not the fixed image. In this case, it is questionable whether it is proper to align the tumor boundary. Alg. B (SSTVD) also visually produces good agreement of the lung boundary and vasculature. This tumor surrounds several large airways in the central portion of the tumor, which are also registered well by both algorithms. Alg. B, however, did not produce exact alignment of the tumor boundary, which is more in line with expected performance in the case of infiltrative regression. Results were visually similar in the other two subjects, but are not displayed here.

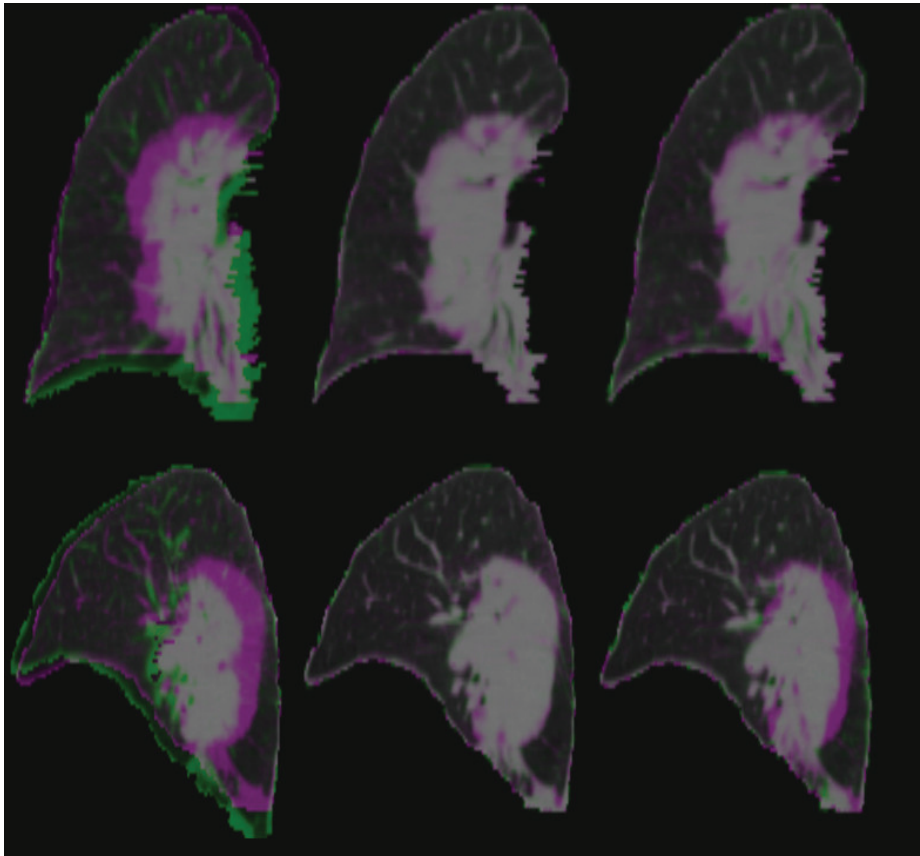


Fig. 2. Complementary color overlays of fixed image (maroon) and moving image (green) of Subject 1. The top row shows coronal slices through the tumor-bearing lung, and the bottom row shows sagittal slices. Left to right: unregistered, after registration with Algorithm A, after registration with Algorithm B.

Fig. 3 shows images of the Jacobian for both algorithms for all three subjects. In each case, Alg. A showed compression in most regions of the tumor. This result is due to the algorithm trying to elastically compress both the region of new parenchyma visible only in the moving image and the tumor itself. Alg. B, on the other hand, shows a Jacobian near unity within the regions of the tumor consistent in both images. The regions where tumor is present in the fixed image, but new parenchyma is visible in the moving image, show expansion of the transform as the algorithm attempts to match the tissue volume in the new parenchyma to the tumor in the fixed image. This result is plausible, as the algorithm does not attempt to match the tumor boundaries but instead is able to account for the differing image content in the two images.

The value of ρ_r was adjusted for both Alg. A and B to determine the effect of increased regularization on matching. Increased ρ_r led to visibly less accurate boundary matching, but the deformation patterns and Jacobian images for each algorithm did not change appreciably.

Table 1 shows the landmark errors prior to and after registration for both algorithms, averaged over all three patients. The errors are listed for all landmarks within a distance d of the tumor surface on the fixed image. The difference in landmark error distributions between SSD and SSTVD was not significant at any value of d , with p ranging from $[0.25, 0.37]$ (Wilcoxon signed rank test). Landmark error was similar between patients, with mean error for SSD of 3.3 (2.5), 3.3 (2.7), and 3.1 (2.4) mm for Subjects 1, 2, and 3, respectively. Landmark error for SSTVD was 3.4 (2.3), 3.4 (2.7), and 3.2 (2.4) mm for the three subjects.

Table 1. Landmark error (mm) prior to and after registration, averaged over all three patients. Errors are reported as mean (standard deviation) for all landmarks within a distance d mm from the tumor surface. N is the number of landmarks within the distance d .

d	N	unregistered	Alg. A (SSD)	Alg. B (SSTVD)
5	3	10.3 (2.3)	4.6 (3.9)	5.9 (3.6)
10	8	9.8 (3.4)	3.9 (2.6)	5.9 (3.8)
15	17	9.4 (3.2)	3.7 (2.0)	4.6 (3.0)
20	27	9.2 (3.2)	3.3 (2.1)	4.1 (2.9)
40	51	8.8 (3.3)	3.2 (2.2)	3.6 (2.6)
All	300	8.3 (3.3)	3.2 (2.5)	3.3 (2.4)

4 Discussion

The goal of this study was to evaluate two different ways to implement intensity cost for registering intra-subject CT acquired during radiotherapy, specifically for infiltrative type tumor regression. The plausibility of the transformations

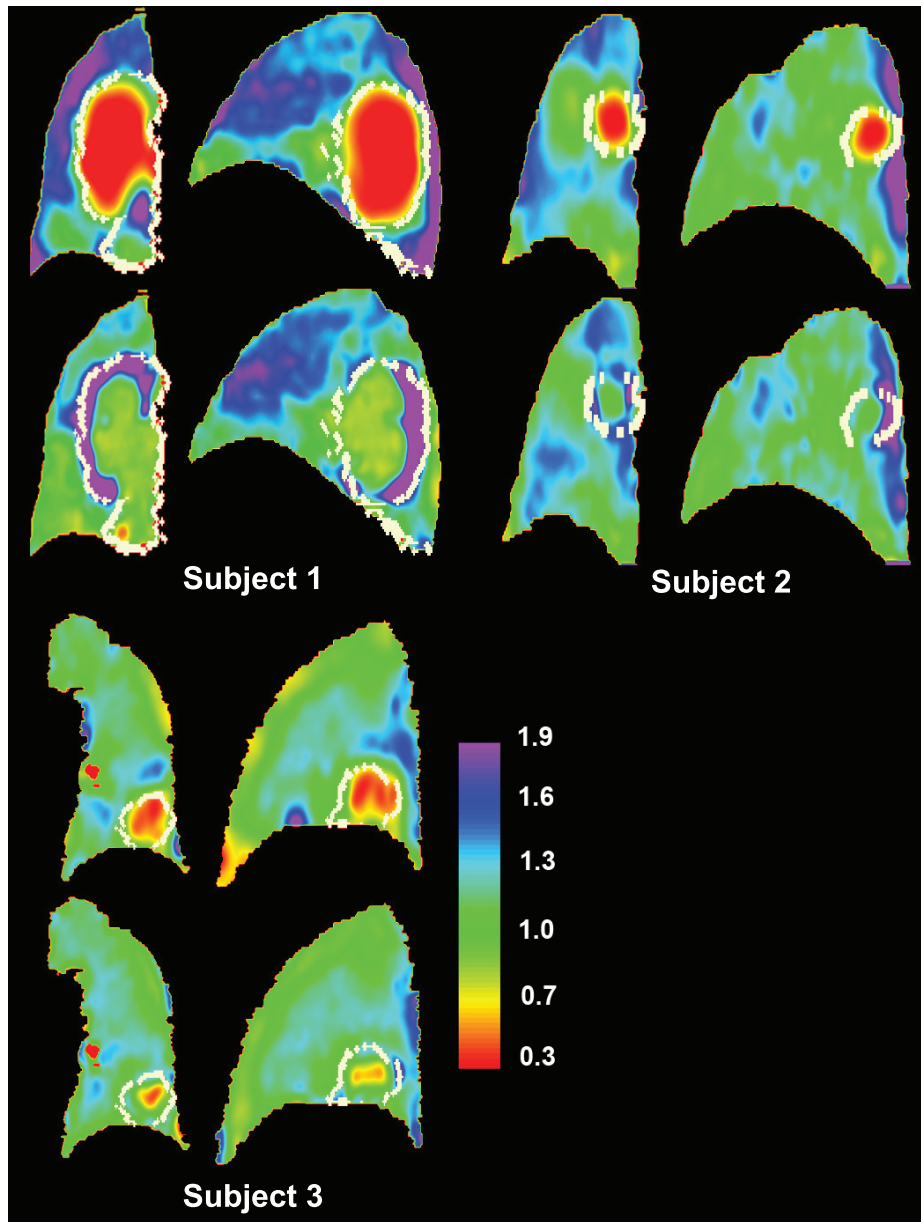


Fig. 3. Images of the Jacobian for the three subjects. Top row in each cluster: Algorithm A. Bottom row in each cluster: Algorithm B. Left column in each cluster: coronal slice of tumor-bearing lung. Right column in each cluster: sagittal slice. A Jacobian less than one (red to yellow color) implies compression of the transformation locally, whereas a Jacobian greater than one (blue to purple color) implies expansion. A Jacobian of unity implies neither expansion nor contraction (green color). The tumor boundary is shown by the white markers.

was assessed by visual inspection of the Jacobian of each transformation. Alg. A (SSD) tended to produce a compression within the tumor, in order to match the smaller tumor on the mid-treatment image to the larger tumor on the planning image. This result is reasonable if the tumor has regressed elastically, and the border contains corresponding tissue in the two images. However, in infiltrative type regression, the tumor tissue at the border has disappeared, replaced by newly-visible lung parenchyma. In this case, the result of Alg. A is inconsistent with the infiltrative hypothesis.

To understand the results from Alg. B (SSTVD), it is helpful to consider three regions of the image. In regions that contain lung parenchyma in both images, SSTVD matches tissue volume as it was designed to do. Changes in the same subject breath hold level between CT acquisitions results in different brightness due to varying voxel air content. In this region, the SSTVD cost assists in matching parenchyma regions while the SSVMD cost matches vessel-like features. In regions containing tumor tissue in both images, intensity content inside the tumor was used for matching. Even though the tumor decreased in size, because this size decrease was due to mass loss, the tumor intensity remained similar in both images. Thus, the SSTVD cost did not try to expand or compress the transform in this region but instead allowed intensity features to drive the registration. Essentially, the SSTVD cost acts as a constraint on the Jacobian determinant in this region. In the tumor region, SSVMD was not used due to masking, so it did not contribute to image matching. The third region is the boundary of visible tumor in the planning image which appears as parenchyma in the mid-treatment image. In this region, there is no corresponding content in the image pair. We found that the SSTVD cost tended to produce an expansion in the transform in this region. In the planning image, the intensity in this region is high, whereas in the mid-treatment image it is lower in the corresponding location where newly-visible parenchyma is found. In this case, the SSTVD cost tends to try to expand the transform to increase the tissue volume in the mid-treatment image. However, the regularization acts to reduce the allowable expansion and compression in this region. Finally, since this region contains no vessel features in the planning image, the SSVMD cost does not affect the matching in this region.

Both SSD and SSTVD produced reasonable, but not subvoxel, accuracy in the normal lung tissue near the tumor. SSD had higher, but not significant, accuracy for landmarks independent of distance from the tumor. Potential solutions to improve the accuracy include increasing the weighting of the SSVMD cost and adding other features such as airways and/or fissures, although neither option was not evaluated here. Within the central regions of the tumor, both algorithms produced reasonable results for the few visible features there, although we did not quantify landmark error in such regions. In conventional CT, such an evaluation is difficult due to the lack of strong features in most tumors. Options to solve this problem include contrast-enhanced CT and/or morphological MRI. Another limitation of the study was the limited cohort size, although a larger study is planned.

5 Conclusions

Two algorithms, both with a pulmonary vessel feature cost and linear elastic regularization, but with different implementations of intensity cost, were evaluated on the problem of intra-subject CT registration during radiotherapy. Both algorithms provided accurate registration, but sum of square tissue volume difference produced more plausible transforms to manage infiltrative type regression. More work is needed to improve accuracy and to validate the registration near the tumor boundary.

Acknowledgments. We would like to thank K. Murphy and B. van Ginneken for use of the IX software. Research reported in this publication was supported by the National Cancer Institute of the National Institutes of Health under Award Numbers R01CA166119 and R01CA166703. The content is solely the responsibility of the authors and does not necessarily represent the official views of the National Institutes of Health.

References

1. Fox, J., Ford, E., Redmond, K., Zhou, J., Wong, J., Song, D.Y.: Quantification of tumor volume changes during radiotherapy for non-small-cell lung cancer. *International Journal of Radiation Oncology, Biology, Physics* **74**(2) (Jun 2009) 341–8
2. Glide-Hurst, C.K., Gopan, E., Hugo, G.D.: Anatomic and pathologic variability during radiotherapy for a hybrid active breath-hold gating technique. *International Journal of Radiation Oncology, Biology, Physics* **77**(3) (Jul 2010) 910–7
3. Kupelian, P.A., Ramsey, C., Meeks, S.L., Willoughby, T.R., Forbes, A., Wagner, T.H., Langen, K.M.: Serial megavoltage CT imaging during external beam radiotherapy for non-small-cell lung cancer: observations on tumor regression during treatment. *International Journal of Radiation Oncology, Biology, Physics* **63**(4) (Nov 2005) 1024–8
4. Sonke, J.J., Lebesque, J., van Herk, M.: Variability of four-dimensional computed tomography patient models. *International Journal of Radiation Oncology, Biology, Physics* **70**(2) (Feb 2008) 590–8
5. Hugo, G.D., Weiss, E., Badawi, A., Orton, M.: Localization accuracy of the clinical target volume during image-guided radiotherapy of lung cancer. *International Journal of Radiation Oncology, Biology, Physics* **81**(2) (Oct 2011) 560–7
6. Sonke, J.J., Belderbos, J.: Adaptive radiotherapy for lung cancer. *Seminars in Radiation Oncology* **20**(2) (Apr 2010) 94–106
7. Guckenberger, M., Richter, A., Wilbert, J., Flentje, M., Partridge, M.: Adaptive radiotherapy for locally advanced non-small-cell lung cancer does not underdose the microscopic disease and has the potential to increase tumor control. *International Journal of Radiation Oncology, Biology, Physics* (Apr 2011)
8. Rit, S., Kuijff, H.J., van Kranen, S., van Herk, M., Sonke, J.J.: Computer assisted analysis of lung tumor regression during radiotherapy. In: *Proceedings of the XVIth International Conference on the use of Computers in Radiation Therapy (ICCR)*. (2010)

9. Ding, K., Bayouth, J.E., Buatti, J.M., Christensen, G.E., Reinhardt, J.M.: 4DCT-based measurement of changes in pulmonary function following a course of radiation therapy. *Medical Physics* **37**(3) (2010) 1261–1272
10. Cao, K., Ding, K., Reinhardt, J.M., Christensen, G.E.: Improving intensity-based lung CT registration accuracy utilizing vascular information. *International Journal of Biomedical Imaging* **2012** (Jan 2012) 285136
11. Frangi, A.F., Niessen, W.J., Vincken, K.L., Viergever, M.A.: Multiscale vessel enhancement filtering. In: *Medical Image Computing and Computer-Assisted Intervention (MICCAI'98)*. Springer (1998) 130–137
12. Yin, Y., Hoffman, E.A., Lin, C.L.: Mass preserving nonrigid registration of CT lung images using cubic B-spline. *Medical Physics* **36**(9) (2009) 4213–4222
13. Cao, K., Christensen, G.E., Ding, K., Du, K., Raghavan, M.L., Amelon, R.E., Baker, K.M., Hoffman, E.A., Reinhardt, J.M.: Tracking regional tissue volume and function change in lung using image registration. *International Journal of Biomedical Imaging* **2012** (Jan 2012) 956248
14. Murphy, K., van Ginneken, B., Klein, S., Staring, M., de Hoop, B.J., Viergever, M.A., Pluim, J.P.W.: Semi-automatic construction of reference standards for evaluation of image registration. *Medical Image Analysis* **15**(1) (Feb 2011) 71–84